




DOI: 10.5604/01.3001.0054.3230

Electrochemical corrosion of aluminium alloy AA1050, processed by accumulative roll bonding

M.D. Ilieva *, R.H. Radev

Department of Materials Science and Technology, University of Ruse "Angel Kanchev",
8 Studentska st., POB 7017, Ruse, Bulgaria

* Corresponding e-mail address: mdilieva@uni-ruse.bg

ORCID identifier:  <https://orcid.org/0000-0001-7962-0760> (M.D.I.)

ABSTRACT

Purpose: To investigate the changes in corrosion behaviour of severely deformed by accumulative roll bonding aluminium alloy AA1050.

Design/methodology/approach: To determine the influence of the accumulative roll bonding on microstructure, texture, and grain size, electron backscattered diffraction was used. Corrosion behaviour was evaluated in a 3.5 wt.% sodium chloride water solution using anodic polarisation.

Findings: It was found out that accumulative roll bonding up to eight cycles led to an increase in corrosion rate compared to annealed alloy, but the increase in the number of cycles of accumulative roll bonding from two to eight shows a tendency toward lowering corrosion rates. It has a beneficial influence on pitting corrosion susceptibility.

Research limitations/implications: The presented research focuses only on the influence of texture and grain size on severely deformed aluminium alloy AA1050 corrosion. Other factors, such as accumulated during deformation stresses, could also play their role in the corrosion process.

Originality/value: The paper reports results on the influence of two factors – texture and grain size, on the corrosion of severely deformed aluminium alloy AA1050. Most reports on the topic include only the influence of texture or grain size.

Keywords: Severe plastic deformation, Corrosion, Texture, Grain size, Aluminium alloys

Reference to this paper should be given in the following way:

M.D. Ilieva, R.H. Radev, Electrochemical corrosion of aluminium alloy AA1050, processed by accumulative roll bonding, Archives of Materials Science and Engineering 124/1 (2023) 5-13.
DOI: <https://doi.org/10.5604/01.3001.0054.3230>



PROPERTIES

1. Introduction

Severe plastic deformation (SPD) processes are used for structure refinement to enhance the mechanical properties of metallic materials. There are different severe plastic

deformation techniques, such as Equal-channel Angle Pressing (ECAP), High Pressure Torsion (HTP), SPD by V-shape die compression, Accumulated Extrusion (Accum EX), Accumulative Roll Bonding (ARB).

ARB gives possibilities to produce multi-layered and multi-composite materials with enhanced strength and toughness [1,2]. During SPD several changes to the structure occur grain refinement in coarse-grained metallic materials through dislocation slip and deformation twinning, together with SPD-induced grain growth in nanostructured metals through grain rotation and grain boundaries migration, changes in twin density and dislocation density, SPD-induced phase transformations that can be diffusive and martensitic, precipitates formation, strain hardening and grain boundaries strengthening, texture, accumulated stress [1, 3-7]. There are many scientific reports on the changes.

The corrosion behaviour of ARB-processed materials has also been investigated in different works [8-13]. From the reported results, it is evident that ARB can have different influences on the corrosion of metallic materials depending on the process parameters, alloy composition, environment composition and conditions.

As ARB causes grain refinement and texture – two factors known to affect corrosion resistance, how they influence the corrosion behaviour of ARB-processed metallic materials is a noteworthy problem.

In this paper, we study the effect of accumulative roll bonding of aluminium alloy AA1050 on the grain size, texture, corrosion behaviour, and the possible relationship between them.

2. Experimental procedure

The tested specimens were prepared of aluminium alloy AA1050. The chemical composition determined from glow discharge optical emission spectroscopy (GDOES) analysis is shown in Table 1.

2.1. Processing samples by ARB

The rough material had been cut into sheets with a length of 200 mm and a width of 60 mm. They were annealed at 520°C for 1 h and then cooled in water. Before the rolling process, the strips were cleaned with a rotary wire brush with a diameter of 40 mm and then stacked two by two together.

The thickness of the stacked strips was 2.4 mm in total. The stacked strips were welded by spot welding at all four corners and then rolled.

The specimens were rolled at the following conditions: room temperature, rolls with a diameter of 90 mm and velocity of 30 rpm, and no preheating or cooling of the specimens or the rolls. After rolling, every new strip was approximately twice as long as the initial strips. The new strips were halved in length to repeat the whole process (brushing, stacking, spot welding, and rolling composed one cycle of ARB), again. It was repeated for up to eight cycles.

2.2. Preparation of ARB samples for microstructural analysis and hardness testing

The tested specimens were cut off by wet abrasive cutting. Then, the specimens were cold-mounted. Wet grinding was used with SiC abrasive paper 800 for 30 s, 1200 for 1 min and 4000 for 2 min. The polishing was carried out in two steps. At first, the samples were polished with 1 µm diamond paste with oil-based lubricant for 5 min. The final polishing was carried out with 0.06 µm silica colloid for 3 min and water for the last 30 s. After the mechanical polishing, a vibratory polishing was carried out using a 0.04 µm colloidal silica solution for approximately 1 hour.

An analytical field emission scanning electron microscope (JEOL JSM-7001F) fitted with electron backscatter diffraction EBSD image detectors was used to collect the experimental data for the microstructural examination. The data were collected using a TexSEM Laboratories TSL orientation imaging system and orientation imaging microscopy OIMTM software at 13 KV. The orientation maps were acquired at a sample tilt of 70° and a working distance of 15 mm. The program identified low-angle grain boundaries as having misorientation angles of 2°–5° and high-angle grain borders as having misorientation discrepancies between consecutive measuring locations greater than 15°.

The hardness values were measured with an FM-300 tester at the following conditions: 100 g load, room temperature, 15 s hold of the indenter. There were 20 measurements for each sample, and the values presented here are the average of these 20 measurements.

Table 1.
Chemical composition of the tested alloy

Chemical components		Chemical composition of ENAW-A199.5 (ENAW-1050A) in wt.%								
		Fe	Si	Mn	Ti	Al	Cu	Mg	Zn	Other
Standard quantity	min	–	–	–	–	99.5	–	–	–	–
	max	0.4	0.25	0.05	0.05	–	0.05	0.05	0.07	0.03
GDOES results		–	–	0.021	0.011	99.8	0.079	0.0089	–	–

2.3. Electrochemical tests

Before electrochemical testing, the samples were cleaned with deionised water and acetone. The analysed surface area was 0.4 cm^2 . Potentiodynamic polarisation studies were performed in an open-air setup containing a 3.5-weight per cent NaCl aqueous solution at ambient temperature. A standard three-electrode cell was used with a saturated calomel electrode (SCE), a Pt-counter electrode, and the studied sample as a working electrode. All potentials were calculated and reported versus standard hydrogen electrodes (SHE). Before polarisation, all specimens were allowed to stabilise for 240 minutes. The scan rate was 1 mV s^{-1} . The polarisation potentials changed from -650 mV/SHE to $+200 \text{ mV/SHE}$. The external polarisation potentials were applied by a potentiostat RADELKIS OH-405. The test data were collected with a USB digital acquisition controller NI USB-6008 and then plotted as graphs. Using ElChemViewer [14], Tafel extrapolation was carried out, and corrosion current densities i_{corr} and corrosion potentials E_{corr} were determined. Corrosion rates CR were calculated according to ASTM G102-89 (2015), ignoring the small quantities of alloying elements (see Tab. 1).

3. Results and discussion

3.1. Results

The microstructure of the annealed alloy is shown in Figure 1. The inverse pole figures (orientation maps, shown in Figures 2 and 3) depict crystallographic directions $\langle hkl \rangle$, aligned with the normal direction (ND). As the studied material had a cubic crystal structure, the inverse pole figures indicate planes $\{hkl\}$, normal to ND, i.e., parallel to the tested surfaces. The correspondence between the colours and the crystallographic directions is indicated in the standard stereographic triangle shown in Figure 2b. The black pixels in Figures 2 and 3 represent non-indexed points.

Figure 1 and Figure 2 show the single-phase random crystal orientation of the annealed sample, with an average grain size of $28.6 \mu\text{m}$. The orientation map of AA1050 after two cycles (Fig. 3a) consists mainly of one colour region. According to the colour triangle, orientation close to $\langle 001 \rangle$ is predominant. The observed average grain size in ND is $10.5 \mu\text{m}$. The orientation map of AA1050 after four cycles (Fig. 3b) shows the orientation of most of the grains has changed towards $\langle 101 \rangle$, with some grains oriented close to $\langle 111 \rangle$.

It is accompanied by a reduction in grain size to an average value of $6.7 \mu\text{m}$. Another crystal orientation change occurred following six ARB cycles, as shown in Figure 3c.

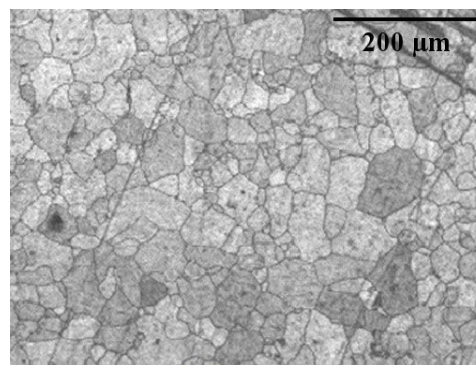


Fig. 1. Microstructure of the annealed AA1050

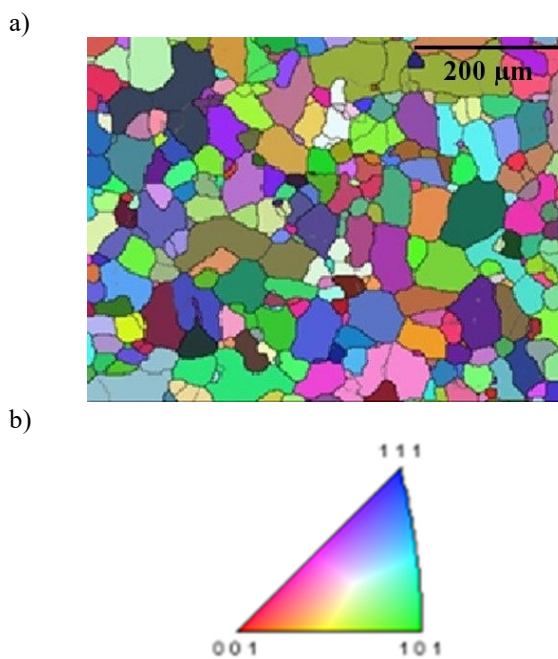


Fig. 2. a) Inverse pole figure of annealed AA1050; b) standard stereographic triangle

The main grain orientation is close to $\langle 001 \rangle$, but quite a few grains have an orientation near $\langle 111 \rangle$. After six cycles of ARB, the average grain size is $2.9 \mu\text{m}$, indicating that the grain size has decreased. The next ARB with eight cycles has led to a negligible grain size reduction. That way, after eight cycles of ARB, the average size of grains is $2.1 \mu\text{m}$. The orientation map (Fig. 3d) demonstrates a main orientation on $\langle 001 \rangle$. The density of non-indexed points decreases with increasing the number of cycles.

Table 2 shows that the ARB technique used here allowed an increase in the hardness of AA 1050 from 26 HV0.1 in annealed condition to 52 HV0.1 after six and eight cycles.

Table 2.
Microstructural, mechanical and corrosion characteristics of tested samples

Sample	Orientation direction	Grain size, μm	HV0.1	E_{ss} , mV	E_{corr} , mV	i_{corr} , $\mu\text{a cm}^{-2}$	CR, mm yr^{-1}
annealed	random	28.60	26	-473	-568	0.205	0.002
2 cycles	$\langle 001 \rangle$; $\langle 111 \rangle$	10.50	48	-482	-596	1.629	0.018
4 cycles	$\langle 101 \rangle$; $\langle 111 \rangle$	6.70	51	-505	-559	1.450	0.016
6 cycles	$\langle 001 \rangle$; $\langle 111 \rangle$	2.90	52	-513	-472	2.248	0.024
8 cycles	$\langle 001 \rangle$	2.10	52	-509	-482	0.469	0.005

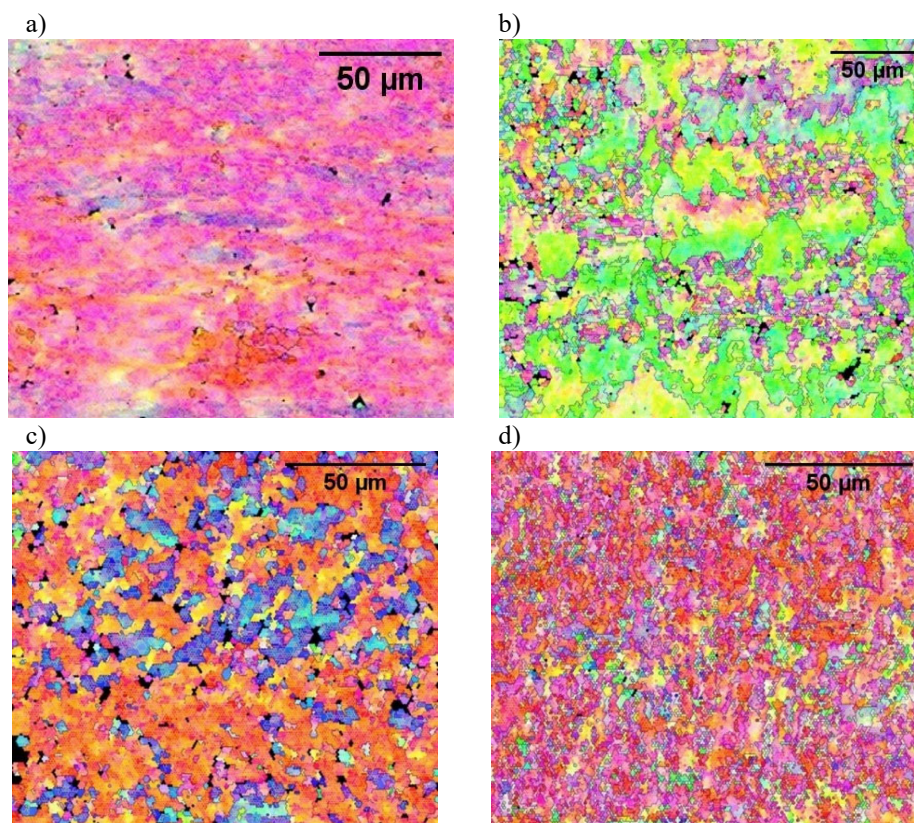


Fig. 3. Inverse pole figures of ARB processed samples after a) 2 cycles, b) 4 cycles, c) 6 cycles, d) 8 cycles

Figure 4 shows how the open circuit potential (OCP) of the tested samples changed with time. The change in OCP of the annealed AA1050 shows an unstable potential with time, not reaching a steady-state value for 240 minutes. The same is true for the sample that was deformed twice. Four, six, and eight cycles of ARB led to a more uniform OCP and allowed AA1050 to reach a steady-state potential. It is interesting to note that the sample that was subjected to six cycles of deformation showed a temporary tendency toward more positive open circuit potential values. The values of the steady-state potential E_{ss} are given in Table 2 for specimens after four, six and eight cycles. Table 2 gives the potential

values at the end of the 240 minutes for the annealed specimen and the specimen after two cycles.

Figure 5 illustrates the behaviour of the tested samples during anodic polarisation. The obtained potentiodynamic curves (PDC) allow the splitting of the specimens into two groups: 1) annealed, two cycles and four cycles, and 2) six cycles and eight cycles. The PDCs of the first group demonstrate a more negative corrosion potential (E_{corr}). The corresponding values of E_{corr} are shown in Table 2, together with those of corrosion current density i_{corr} , steady-state potential E_{ss} and corrosion rate CR. As a result of the polarisation, pits were formed on all tested specimens.

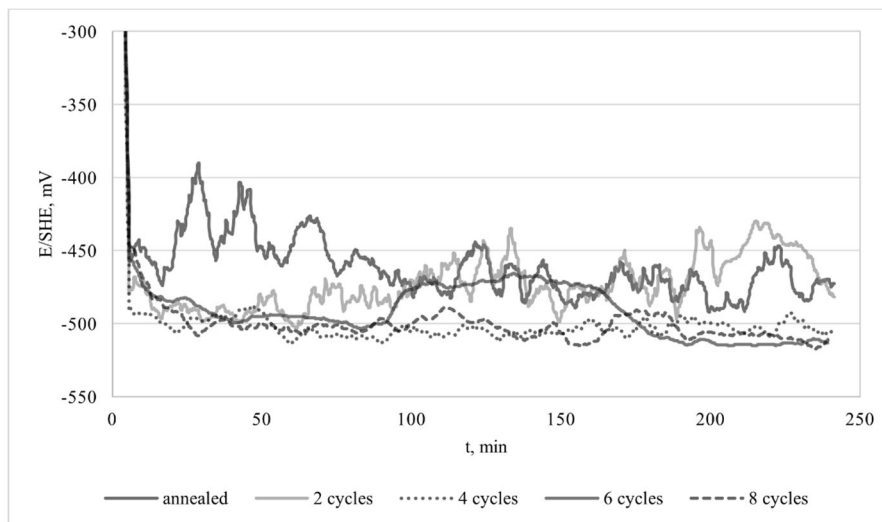


Fig. 4. Open circuit potential change with time of tested samples in 3.5 wt.% NaCl

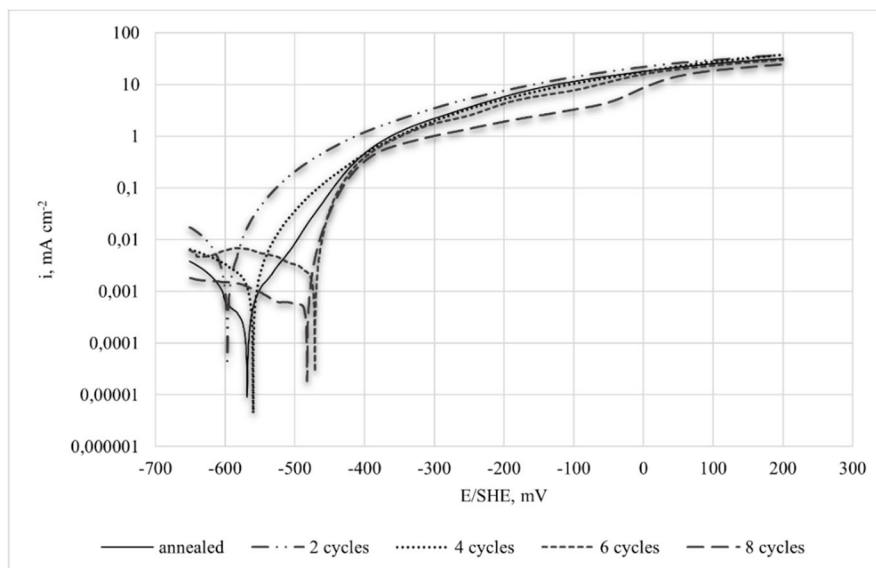


Fig. 5. Potentiodynamic curves of anodic polarisation of tested samples in 3.5 wt.% NaCl

3.2. Discussion

Some of the effects of severe plastic deformation are studied in this work, including texture and grain size reduction. Both play an important role in the corrosion behaviour of metallic materials.

The interaction of a thin Al_2O_3 passive layer with the environment governs aluminium's and its alloys' tendency to corrosion. As the refined structure provides more sites (grain boundaries, dislocations) for the passive layer to form, the layer on such a structure should be denser, having more sites

to form. It is known [15] that the changes in grain size have an ambiguous influence on corrosion rate depending on the corrosive medium. In the present experiment, the specimens were tested in a medium with oxygen that favours the formation of a natural oxide layer. Thus, according to [15,16], one should expect a decrease in corrosion rate with grain refinement.

At the same time, chloride ions are known to incorporate into the oxide layer and destroy it at local sites, leading to pit formation. It is suggested in the scientific literature that a depassivating medium grain size reduction leads to an

increase in corrosion rate. Suppose the corrosive medium acts as a passivator and a de-passivator simultaneously. In that case, a finer grain structure increases the uniform corrosion rate and decreases the localised corrosion rate [15,16].

As Vargel [17] states, the potential measured during electrochemical tests on aluminium and its alloys is a mixed potential between the oxide film and the underlying metal. So, when interpreting the electrochemical behaviour of aluminium and its alloys, it is necessary to analyse the impact the structure has on the stability of the passive layer.

Numerous experiments were conducted to assess the impact of grain orientation on metallic materials' electrochemical behaviour [18-27]. For aluminium, it is found out that texture on {111} planes flavours pits formation, while {110} and {100} planes are less susceptible to pitting corrosion. Aluminium has a face-centred cubic structure, and the atomic planar density in this structure increases in the order $\{110\} < \{100\} < \{111\}$, with a planar density of 8.5 atoms nm^{-2} , 12.2 atoms nm^{-2} , and 14.1 atoms nm^{-2} , respectively. As planar density increases, the surface energy decreases, and one should expect lower corrosion rates. However, when studying aluminium alloys and other passivating metals, it is necessary to consider the influence the planar density has on the passive layer formation and its stability. Higher planar density means lower atomic activities, thus difficulty in oxide layer formation.

The coordination of the surface atoms affects the coherence/incoherence between the metallic atoms and the atoms in the oxide layer upon them. In the case of aluminium, the spontaneously formed Al_2O_3 layer is amorphous [17,23]. Thus, the boundary "metal/oxide layer" accommodates some strain and stresses. As stated in [23], a layer formed on an elastically soft substrate is more stable and accommodates lesser stresses than on an elastically hard surface. The biaxial elastic modulus for {110}, {100}, and {111} of aluminium was calculated and is reported in [23]. The report shows higher biaxial elastic modulus for {111} and lower – for {100}. Hence, the oxide layer formed on {100} is the most stable, and the one on {111} would be

readily dissolved. Based on [23], a coefficient M , a measure of the elastic strain energy for {110}, {100}, and {111} aluminium planes, was calculated by Seo et al. [26]. It was reported that {111} planes of Al had higher elastic strain energy, but {110} and {100} had close strain energies, with {100} having the lowest.

This way, the stability of the oxide layer is connected to the crystal orientation of the underlying metal – on top of the densest plane, a layer with the lowest stability is formed. Furthermore, it is suggested in [20] that the higher pitting corrosion rates for {111} aluminium plane result from the higher number of atoms on a smaller area, available for electrochemical reactions. Hence, higher corrosion rates should be expected on the densest atomic plane {111}, and corrosion rates on {100} and {110} should be around the same. The information, taken from scientific literature, is summarised in Table 3.

Given the above facts, the following interpretation of the reported results can be made.

As the results show in Table 2, the most pronounced effect of grain boundary strengthening was recorded after two cycles of ARB when Vickers hardness increased almost twice. Considering the nearly twofold reduction in grain size, it follows the Hall–Petch relation but also indicates the stresses present in the deformed alloy.

Following two cycles of ARB, the corrosion current density increased by one order of magnitude. After two cycles of ARB, the alloy did not reach a steady-state potential during the 240-minute stabilisation. The fact shows that the oxide layer was not stabilised before polarisation, comparable to the annealed alloy. During initial cathodic polarisation below corrosion potential, a cathodic reaction showed greater rates, activating the surface for the next pitting formation. It should be noted that for aluminium and its alloys, the corrosion potential equals the pitting potential, and the corrosion current density could not be taken as a measure of pitting susceptibility but rather as a measure of global corrosion rate [17]. As potentiodynamic curves do not allow for differentiation between uniform and pitting corrosion rates, the calculations in Table 2 are overall corrosion rates.

Table 3.
Some characteristics of aluminium main atomic planes

Plane	*Calculated planar density, atoms nm^{-2}	Surface energy, J m^{-1} [24]	Biaxial elastic modulus, GPa [23]	** M , GPa [26]	Expected pitting corrosion rate
110	8.5	0.97	109.449	104.7	close to {100}
100	12.2	0.93	98.418	101	lowest
111	14.1	0.939	113.267	114.9	highest

*Calculated in the present work, assuming the parameter of the fcc Al-lattice equals 0.405 nm.

**Higher M means higher elastic strain energy at the same strain.

It follows the stated in [15,16] that a decrease in grain size results in a rise in uniform corrosion rate in an environment with an active-passive effect on the metallic surface.

Nevertheless, the corrosion potential, coinciding with the pitting potential, demonstrates pitting susceptibility lower than that of the annealed specimen. As the grain orientation after two cycles exposed to the surface mainly the less susceptible to dissolution planes {001}, the corrosion behaviour following two cycles of ARB was governed by the grain size reduction and the stresses accumulated during deformation. Such stresses caused flaws in the oxide layer, serving as sites for the initiation of corrosion processes.

Following four cycles of ARB, AA1050 demonstrated similar hardness value and corrosion current density (corrosion rate), with pitting potential close to that of the annealed specimen. The sample that was subjected to four cycles of ARB is distinguished from the rest as the only one showing a {110} orientation. The texture on {110} and the reduction in grain size after four cycles of ARB did not lead to a significant change in corrosion current density, indicating that these are not the only factors affecting corrosion behaviour. Interpreting the results, the stresses built up during deformation should be considered, too.

The almost tenfold (compared to the annealed alloy) reduction in grain size and the reappearance of {100} orientation after six cycles of ARB did cause the corrosion current density to rise and to a positive shift of corrosion (pitting) potential. The fact shows an increase in pitting corrosion resistance, i.e., the plane orientation that impedes pitting formation affected the susceptibility to pitting corrosion positively but did not overcome the reduction in grain size to lower the current corrosion density. As the values of the Vickers hardness, measured after six and eight cycles, corresponding to the steady-state grain size associated with the annihilation of dislocations [28], dynamic recovery also had some merit for the positive shift in pitting potential.

After eight cycles of ARB, the non-indexed points in the orientation map almost disappeared; it is a sign of a perfect crystal lattice, thus, a more perfect, less stressed oxide film formed. It is shown as a decrease in the corrosion current density of the specimen subjected to eight cycles of ARB. Moreover, the specimen's crystallographic orientation {100} is supposed to impede its pitting corrosion, so the corrosion (pitting) potential is shifted in a positive direction. The reduction of grain size after eight cycles of ARB was negligible compared to the grain size after six cycles of ARB, indicating a steady-state grain size was achieved due to the processes of dynamic recrystallisation that expended

the energy accumulated during previous cycles. It also suggests a less stressed oxide layer formed after eight ARB cycles. Thus, the corrosion current density decreased by one order of magnitude, approaching that of the annealed alloy but still higher.

4. Conclusions

The electrochemical behaviour of the tested specimens is influenced by factors acting in different directions. When comparing the deformed AA1050 with the annealed AA1050, the grain size reduction does lead to an increase in the corrosion rate of AA1050 after two, four, six, or eight cycles of ARB in a 3.5 wt.% NaCl water solution. The same goes for the preferred crystallographic orientation. Nevertheless, the corrosion current density (corrosion rate, respectively) and the pitting susceptibility of severely deformed AA1050 tend to decrease with the number of cycles. Following six and eight cycles of ARB, AA1050 is less susceptible to pitting corrosion and demonstrates a more positive pitting potential than the annealed AA1050. In conclusion, the results lean toward recommending eight cycles of accumulative roll bonding of aluminium alloy AA1050 as a treatment for hardness increase that does not worsen the corrosion resistance of the alloy.

The observed changes in corrosion rate and pitting susceptibility (corrosion/pitting potential) cannot be attributed to the effects of grain refinement or to crystallographic orientation only. The analysis of the results touches on how other factors, such as stress and strain accumulation and dynamic recrystallisation, play their role in forming a stable passive layer and the dissolution of the metal. The analysis emphasises the need for further research to refine the understanding of an optimal number of accumulative roll bonding for a simultaneous increase in the mechanical and corrosion performance of metallic materials. The knowledge of the influence of the factors on the corrosion and mechanical behaviour of severely deformed metallic materials would allow the design of proper technological processes for manufacturing materials that combine enhanced mechanical properties and corrosion resistance in a specific aggressive environment.

Acknowledgements

The work was funded by project №2023-MTF-01, supported by the Science Fund at Ruse University “Angel Kanchev”, Bulgaria.

References

- [1] Y. Cao, S. Ni, X. Liao, M. Song, Y. Zhu, Structural evolutions of metallic materials processed by severe plastic deformation, *Materials Science and Engineering: R: Reports* 133 (2018) 1-59. DOI: <https://doi.org/10.1016/j.mser.2018.06.001>
- [2] M. Ebrahimi, Q. Wang, Accumulative roll-bonding of aluminum alloys and composites: An overview of properties and performance, *Journal of Materials Research and Technology* 19 (2022) 4381-4403. DOI: <https://doi.org/10.1016/j.jmrt.2022.06.175>
- [3] M. Koralnik, B. Adamczyk-Cieślak, M. Kulczyk, J. Mizera, The effect of deformation degree on the microstructure of the 6060 aluminium alloy, *Archives of Materials Science and Engineering* 85/2 (2017) 80-85. DOI: <https://doi.org/10.5604/01.3001.0010.3429>
- [4] J. Hirisch, Texture and anisotropy in industrial, *Archives of Metallurgy and Materials* 50/1 (2005) 21-34.
- [5] P. Snopiński, T. Tański, O. Hilšer, A. Lubos, Effect of ECAP process on structure and hardness of AlMg3 aluminium alloy, *Archives of Materials Science and Engineering* 84/2 (2017) 79-85. DOI: <https://doi.org/10.5604/01.3001.0010.0982>
- [6] M. Karoń, A. Kopyś, M. Adamiak, J. Konieczny, Microstructure and mechanical properties of the annealed 6060 aluminium alloy processed by ECAP method, *Archives of Materials Science and Engineering* 80/1(2016) 31-36. DOI: <https://doi.org/10.5604/18972764.1229616>
- [7] P. Snopiński, T. Tański, K. Labisz, S. Rusz, P. Jonsta, M. Król, Wrought aluminium-magnesium alloys subjected to SPD processing, *International Journal of Materials Research* 107/7 (2016) 637-645. DOI: <https://doi.org/10.3139/146.111383>
- [8] M. Vakili, E. Borhani, A. Ashrafi, Corrosion Behavior of Nano-/Ultrafine-Grained Al-0.2 wt.% Sc Alloy Produced by Accumulative Roll Bonding (ARB), *Journal of Materials Engineering and Performance* 27 (2018) 4253-4260. DOI: <https://doi.org/10.1007/s11665-018-3489-1>
- [9] W. Wei, K. Xia Wei, Q.B. Du, Corrosion and tensile behaviors of ultra-fine grained Al-Mn alloy produced by accumulative roll bonding, *Materials Science and Engineering: A* 454-455 (2007) 536-541. DOI: <https://doi.org/10.1016/j.msea.2006.11.063>
- [10] M.M. Taherian, M. Yousefpour, E. Borhani, The effect of ARB process on corrosion behavior of nano-structured aluminum alloys in Na₂HPO₄·12H₂O and Zn(NO₃)₂·6H₂O PCMs, *Engineering Failure Analysis* 107 (2020) 104222. DOI: <https://doi.org/10.1016/j.engfailanal.2019.104222>
- [11] S. Pashangeh, M. Alizadeh, R. Amini, Structural and corrosion behavior investigation of novel nano-quasicrystalline Al-Cr-Fe reinforced Al-matrix composites produced by ARB process, *Journal of Alloys and Compounds* 890 (2022) 161774. DOI: <https://doi.org/10.1016/j.jallcom.2021.161774>
- [12] A. Fattah-alhosseini, S.O. Gashti, Corrosion Behavior of Ultra-fine Grained 1050 Aluminum Alloy Fabricated by ARB Process in a Buffer Borate Solution, *Journal of Materials Engineering and Performance* 24/9 (2015) 3386-3393. DOI: <https://doi.org/10.1007/s11665-015-1627-6>
- [13] S.O. Gashti, A. Fattah-alhosseini, Y. Mazaheri, M.K. Keshavarz, Microstructure, mechanical properties and electrochemical behavior of AA1050 processed by accumulative roll bonding (ARB), *Journal of Alloys and Compounds* 688B (2016) 44-55. DOI: <https://doi.org/10.1016/j.jallcom.2016.07.177>
- [14] J. Hrbac, V. Halouzka, L. Trnkova, J. Vacek, eL-Chem Viewer: A Freeware Package for the Analysis of Electroanalytical Data and Their Post-Acquisition Processing, *Sensors* 14/8 (2014) 13943-13954. DOI: <https://doi.org/10.3390/s140813943>
- [15] S. Gollapudi, Grain size distribution effects on the corrosion behaviour of materials, *Corrosion Science* 62 (2012) 90-94. DOI: <https://doi.org/10.1016/j.corsci.2012.04.040>
- [16] K. Ralston, N. Birbilis, C. Davies, Revealing the relationship between grain size and corrosion rate of metals, *Scripta Materialia* 63/12 (2010) 1201-1204. DOI: <https://doi.org/10.1016/j.scriptamat.2010.08.035>
- [17] C. Vargel, *Corrosion of Aluminium*, 2nd Edition, Elsevier, Amsterdam, 2020. DOI: <https://doi.org/10.1016/C2012-0-02741-X>
- [18] G.M. Treacy, C.B. Breslin, Electrochemical studies on single-crystal aluminium surfaces, *Electrochimica Acta* 43/12-13 (1998) 1715-1720. DOI: [https://doi.org/10.1016/S0013-4686\(97\)00305-8](https://doi.org/10.1016/S0013-4686(97)00305-8)
- [19] P.T. Brewick, N. Kota, A.C. Lewis, V.G. DeGiorgi, A.B. Geltmacher, S.M. Qidwai, Microstructure-sensitive modeling of pitting corrosion: Effect of the crystallographic orientation, *Corrosion Science* 129 (2017) 54-69. DOI: <https://doi.org/10.1016/j.corsci.2017.09.009>
- [20] B. Davis, P.J. Moran, P.M. Natishan, Metastable pitting behavior of aluminum single crystals, *Corrosion Science* 42/12 (2000) 2187-2192. DOI: [https://doi.org/10.1016/S0010-938X\(00\)00032-9](https://doi.org/10.1016/S0010-938X(00)00032-9)
- [21] X. Zhang, X. Zhou, T. Hashimoto, B. Liu, Localized corrosion in AA2024-T351 aluminium alloy: transition from intergranular corrosion to crystallographic pitting,

- Materials Characterization 130 (2017) 230-236. DOI: <https://doi.org/10.1016/j.matchar.2017.06.022>
- [22] Y. Takayama, K. Nohara, H. Kato, Influence of Crystallographic Orientation on Corrosion Behavior of 5N Purity Aluminum, Proceedings of the 12th International Conference on Aluminium Alloys, Yokohama, Japan, 2010, 1469-1474.
- [23] J.-H. Jeong, C.-H. Choi, D.N. Lee, A model for the <100> crystallographic tunnel etching of aluminium, Journal of Materials Science 31 (1996) 5811-5815. DOI: <https://doi.org/10.1007/BF01160833>
- [24] L. Fan, H. Lu, J. Leng, Z. Sun, C.C. Chen, The effect of crystal orientation on the aluminum anodes of the aluminum–air batteries in alkaline electrolytes, Journal of Power Sources 299 (2015) 66-69. DOI: <https://doi.org/10.1016/j.jpowsour.2015.08.095>
- [25] W. Wang, A. Alfantazi, Correlation between grain orientation and surface dissolution of niobium, Applied Surface Science 335 (2015) 223-226. DOI: <https://doi.org/10.1016/j.apsusc.2015.01.208>
- [26] J.H. Seo, J.-H. Ryu, D.N. Lee, Formation of crystallographic etch pits during ac etching of aluminum, Journal of The Electrochemical Society 150/ 9 (2003) B433. DOI: <https://doi.org/10.1149/1.1596952>
- [27] M. Yasuda, F. Weinberg, D. Tromans, Pitting Corrosion of Al and Al-Cu Single Crystals, Journal of The Electrochemical Society 137/12 (1990) 3708. DOI <https://doi.org/10.1149/1.2086291>
- [28] T. Hebesberger, H.P. Stüwe, A. Vorhauer, F. Wetscher, R. Pippan, Structure of Cu deformed by high pressure torsion, Acta Materialia 53/2 (2005) 393-402. DOI: <https://doi.org/10.1016/j.actamat.2004.09.043>



© 2023 by the authors. Licensee International OCSCO World Press, Gliwice, Poland. This paper is an open-access paper distributed under the terms and conditions of the Creative Commons Attribution-NonCommercial-NoDerivatives 4.0 International (CC BY-NC-ND 4.0) license (<https://creativecommons.org/licenses/by-nc-nd/4.0/deed.en>).